Geophysical Journal International

Spectrum of strong-motion records for large magnitude Chilean earthquakes

Journal:	*Geophysical Journal International*
Manuscript ID	GJI-S-20-0614.R3
Manuscript Type:	Research Paper
Date Submitted by the Author:	n/a
Complete List of Authors:	Rivera, Efrain; Universidad de Chile, Departamento de Geología; Universidad de Chile, Departamento de Geofísica Ruiz, Sergio; Universidad de Chile, Departamento de Geofísica Madariaga, Raúl; Ecole Normale Superieure, Laboratoire de Géologie, Centre National de la Recherche Scientifique; Universidad de Chile, Departamento de Geofísica
Keywords:	Earthquake dynamics < SEISMOLOGY, Earthquake source observations < SEISMOLOGY, Earthquake ground motions < SEISMOLOGY, Fourier analysis < GEOPHYSICAL METHODS

Spectrum of strong-motion records for large magnitude Chilean earthquakes

Efraín Rivera [1, 2], Sergio Ruiz [2] and Raúl Madariaga [2,3]

[1]Departamento de Geología, Universidad de Chile, Plaza Ercilla, Santiago, Chile. E-mail: efrain@u.uchile.cl

[2]Departamento de Geofísica, Universidad de Chile, Blanco Encalada 2002, Santiago, Chile.

[3]Laboratoire de Géologie, PSL Université, Ecole Normale Supérieure and CNRS, 24 rue Lhomond,75230 Paris Cedex 05, France.

Abstract

We studied the broad-band spectra of the 8 largest earthquakes that have occurred in Chile in the last 25 years using strong-motion records and 1-Hz high-rate GNSS (cGNSS) data. To avoid the numerical instability problem with the double integration of the accelerograms, we computed velocity spectra integrating the acceleration time series in the spectral domain and compared them to time-differentiated the cGNSS displacement records. To compute the velocity spectrum, we used a multitaper algorithm so as to provide stability over the entire spectral band. We found that the velocity spectra of records obtained close to the main rupture of the earthquakes are different from classical Aki and Brune spectra. The velocity spectrum of large events in Chile presents a flat trend at low frequencies produced by the near-field waves. This trend converges at low frequencies to the static displacement as determined from GNSS data. For different magnitude earthquakes, we observe a transition in the ground-velocity spectrum from a decay of f^{-1} at high frequencies and a flat trend at low frequencies to a more classical model with a peak at the corner frequency. The source-station distance influences the shape of the velocity spectrum at low frequencies, but there is no simple rule for the records available at present. At intermediate frequencies, the spectra are controlled by surface waves and S waves. We found a transition in the velocity spectrum for the 2014 Iquique earthquake, which indicates a change in the decay of the spectrum for stations at distances greater than ~200 km. Finally, we show that the flat low-frequency trend of the velocity spectra determined from accelerograms, and the peak ground-displacement (PGD) determined from GNSS data scales with the moment to the power 2/3.

Key words: Earthquakes ground-motions; Earthquake source observations; Fourier analysis

1. Introduction

The far-field seismic source spectrum was introduced in the late 1960s and early 1970s (Aki, 1967; Wyss and Brune, 1968; Brune, 1970). Based on this spectrum, Aki (1967) proposed the earthquake scaling law, and Brune (1970) developed his classical f^{-2} model, with a corner frequency that depends on the size of the fault. Several studies have corroborated this spectral model for events recorded in the far-field or small earthquakes recorded close to the epicenter (Abercrombie, 1995; Prieto et al., 2004; Shearer et al., 2006; Allmann and Shearer, 2007). The Aki-Brune model is widely used for the simulation of synthetic seismograms or accelerograms, and for the prediction of strong ground-motion for earthquake engineering purposes.

The observation of earthquakes in the near-field, at short distances from large sources, is important for understanding the physics of the seismic source. Towards the middle of the years 2000 the technological advance of GNSS systems and the increase in the sampling rate, permitted the use of high-rate GNSS records as low-frequency seismograms (Larson et al., 2003; Bock et al., 2004; Ji et al., 2004; Elósegui et al., 2006; Larson, 2009 Vigny et al., 2010; Ruiz et al., 2012; Wang et al., 2013; among others.), making them an excellent complement to the accelerometers when both are installed at very close distances to each other (Emore et al., 2007). The spectrum of these near-field recordings of large earthquakes is different from the f^{-2} model not only at low frequencies but in the entire recorded spectral range (Vidale et al., 1995; Madariaga et al., 2019).

Studies of broad-band spectra of large magnitude Chilean earthquakes ($M_w > 7.5$) in the near-field (hypocentral distance lesser than 300 Km) are scarce. Lancieri et al. (2012) studied the scaling laws for the 2007 Tocopilla earthquake and its aftershocks using acceleration data from strong-motion stations located near the rupture area. They observed that the spectra of aftershocks fit well the f^{-2} spectral model, but not the spectra of the main event of M_w7.8. In the near-field the spectra of this event had two corner frequencies delimiting slopes of f^{-1} at intermediate frequencies and f^{-2} at higher frequencies. This kind of double-corner frequency spectra have been observed for many events in California and elsewhere (Archuleta and Ji, 2016 using the NGA-West2 data set for earthquakes of magnitude $3.3 \leq M \leq 5.3$). Recently, Madariaga et al. (2019) reported broad-band near-field spectra for the Iquique 2014 earthquake, showing that the static co-seismic displacement plays a key role in the computation of the source spectrum and influences the amplitude and decay of the spectra. Similar observations have been reported by Rukhapety et al. (2010), and Inbal and Ziv (2020) for several events in Iceland, Taiwan, and Japan.

The purpose of the present paper is to provide quantitative information about the broad-band spectrum of large earthquakes recorded in the near-field in Chile and to describe the common features of the spectrum, beyond the simple models of Vidale et al. (1995) and Madariaga et al. (2019). Our purpose is not to compare the spectra at low-frequency and short distances that can be studied by GNSS, but to consider the entire frequency band-limited by attenuation at high-frequency and accelerogram noise at low frequencies. We demonstrate that all large earthquakes have similar spectral shapes that are fundamentally different from the classical far-field spectral model of Brune and Aki. For this purpose we study the earthquake spectra of the largest earthquakes that have occurred in Chile in recent years (Antofagasta 1995, M_w 8.0; Tarapacá 2005, M_w 7.8; Tocopilla 2007, M_w 7.7; Maule 2010, M_w 8.8; Iquique 2014, M_w 8.2 and its main aftershock M_w 7.6; Illapel 2015, M_w 8.3 and Chiloé 2016, M_w 7.6), analyzing the behavior at both low and high frequencies and comparing, if possible, with spectra from high-rate GNSS records (cGNSS). We recognized a transition in the flat velocity spectrum at low frequencies dominated by the near-field and Brune's far-field velocity spectrum based on two main criteria: (1) the magnitude of the event, observing a transition from a magnitude range of M_w $5.6-6.5$ for a hypocentral distance of ~90 km; (2) the distance from source to the station, for instance for the Iquique 2014 earthquake, this transition is observed from ~350 km. Finally, we show that the low-frequency near-field velocity spectrum and the PGD scales with moment to the power 2/3.

2. Recent large earthquakes in Chile

In Chile, 8 earthquakes of magnitude greater than M_w 7.5 have occurred in the last 25 years, 7 of which occurred in the plate interface between the South American and Nazca plates, and one within the Nazca plate (Figure 1). The source rupture process of each of these earthquakes has been very well studied using different techniques. The first of these events, the 31 July 1995 Antofagasta earthquake (M_w 8.0) occurred in Northern Chile at a depth of 47 km broke the deeper part of the subduction interface and a segment of 180 km along the coast. Delouis et al. (1997) used broadband, accelerometer, and GPS data to model the rupture process. This event was the first to be observed with GPS and InSAR instruments (Ruegg et al., 1996; Chlieh et al., 2004).

Ten years later occurred the 2005 Tarapacá earthquake (M_w 7.8). This earthquake was an intraplate event of intermediate-depth that occurred within the Nazca plate at a depth of 108 km, as estimated by the CSN (Centro Sismológico Nacional of the University of Chile). Delouis and Legrand (2007) used teleseismic records and a permanent strong-motion network in the near-field operated by the Civil Engineering Department of the University of Chile to make a joint inversion, identifying the fault planes and the displacement distribution. Peyrat et al. (2010a), using the same strong-motion data, made a kinematic and dynamic inversion to propose a fault model for this event. A couple of years after this earthquake, a multi-parameter network of seismological stations was deployed in northern Chile, Integrated Plate Boundary Observatory Chile (IPOC), by German, French and Chilean researchers (IPOC 2006).

In 2007 the Tocopilla earthquake (M_w 7.7) occurred in the deeper part of the plate interface of the South American and Nazca plates (~47 Km according to CSN). This was the first earthquake studied after the installation of the IPOC seismological network; it has been widely studied with different techniques and instruments (Delouis et al., 2009; Peyrat et al., 2010b; Fuenzalida et al., 2013; Schurr et al., 2012; Lancieri et al., 2012). Peyrat et al. (2010b) used near-field strong-motion data to perform a kinematic inversion of this earthquake and Lancieri et al. (2012) studied the spectral properties of the main event and its aftershocks.

The 27 February 2010 Maule earthquake was the first Chilean mega-thrust earthquake studied with modern seismological instruments in the Chilean subduction zone (Ruiz and Madariaga, 2018). This mega-earthquake was well recorded in the near-field by GPS stations (Vigny et al., 2011; Moreno et al., 2012) and accelerometers installed by the University of Chile

(Boroschek et al., 2012, Ruiz et al., 2012). The slip distribution had two large asperities with the largest one located to the north of the rupture (Lay et al., 2010; Delouis et al., 2010; Vigny et al., 2011; Moreno et al., 2012; Ruiz et al., 2012).

A large megathrust earthquake hit Iquique on 1 April 2014 with a magnitude M_w 8.2. This event was recorded by an extensive network of broadband, strong-motion, and GPS instruments deployed by IPOC, and the CSN (Leyton et al., 2018; Baez et al., 2018). This earthquake is the best-recorded events in Chile, studied by many authors in the time domain (Ruiz et al., 2014; Kato and Nakagawa, 2014 Schurr et al., 2014; Duputel et al., 2015; Cesca et al., 2016; León-Ríos et al., 2016; Suzuki et al., 2016; among many others). Two days later, it was followed by the largest aftershock (M_w 7.6), located at the southern limit of the rupture area at a depth of 26 km, as reported by the CSN.

In north-central Chile, the Illapel earthquake of magnitude M_w 8.3 occurred on 16 September 2015, breaking a length of approximately 200 km in the Coquimbo region at a shallow depth of 11 km. Ruiz et al. (2016) documented this earthquake. Broadband, strong-motion, and GNSS instruments are available for the study of this event.

Finally, in 2016 took place the Chiloé event (M_w 7.6) in southern Chile, inside the estimated rupture area of the giant Valdivia earthquake of 22 May 1960 (Ruiz et al., 2017; Melgar et al., 2017; Lange et al., 2018). Many other smaller events of magnitude close to 7 have occurred and have been recorded by the National Accelerometric Network of CSN that was deployed in 2012.

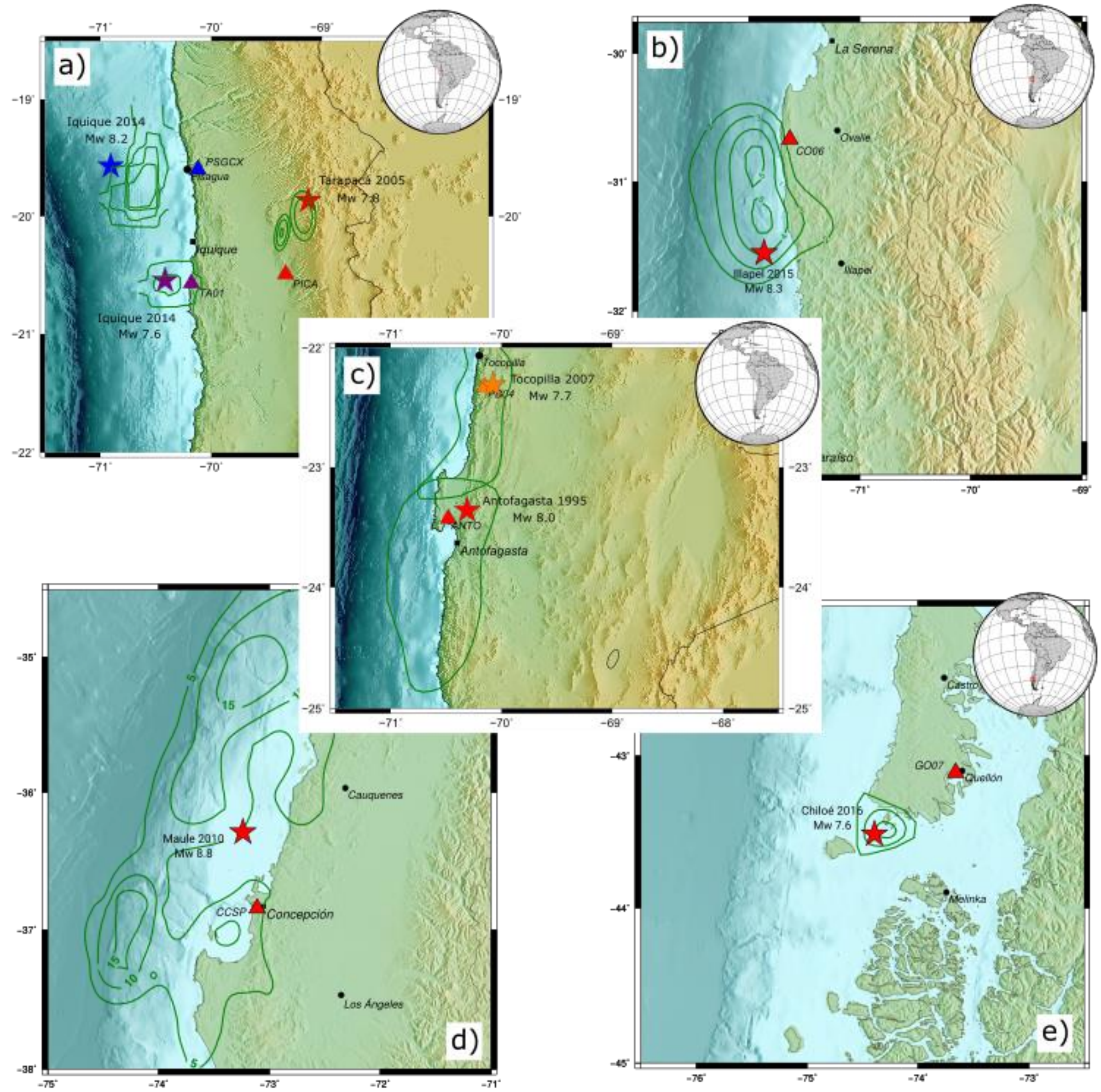

Figure 1. Map with the epicenters of the last 8 earthquakes in Chile and their nearest available acceleration and GNSS stations and the maximum displacements of each earthquake (green contours). **a)** Tarapacá 2005 (Peyrat et al., 2010a), Iquique 2014 and main aftershock (Ruiz et al., 2014); **b)** Illapel 2015 (Ruiz et al., 2016); **c)** Antofagasta 1995 (Delouis et al., 1997) and Tocopilla 2007 (Peyrat et al., 2010b); **d)** Maule 2010 (Vigny et al., 2011); **e)** Chiloé 2016 (Ruiz et al., 2017). Triangles correspond to the GNSS and/or strong-motion station.

3. Data and Methods

We studied the spectra of the major earthquakes that have occurred in Chile in the last 25 years (listed in Table S1): Antofagasta 1995 (M_w 8.0), Tarapacá 2005 (M_w 7.8), Tocopilla 2007 (M_w 7.7), Maule 2010 (M_w 8.8), Iquique 2014 (M_w 8.2), Iquique 2014 (M_w 7.6), Illapel 2015 (M_w 8.3) and Chiloé 2016 (M_w 7.6). We used all the near-field strong-motion stations available (see Table S2). To compute the spectra of these earthquakes, we used strong-motion and collocated GNSS records. For most of the records, it was not possible to separate the P and S waves to study them individually, because the difference in arrival times of P and S waves were too small with respect to the duration of the events (see Figure 2) and because it was difficult to separate near-field surface waves from body waves.

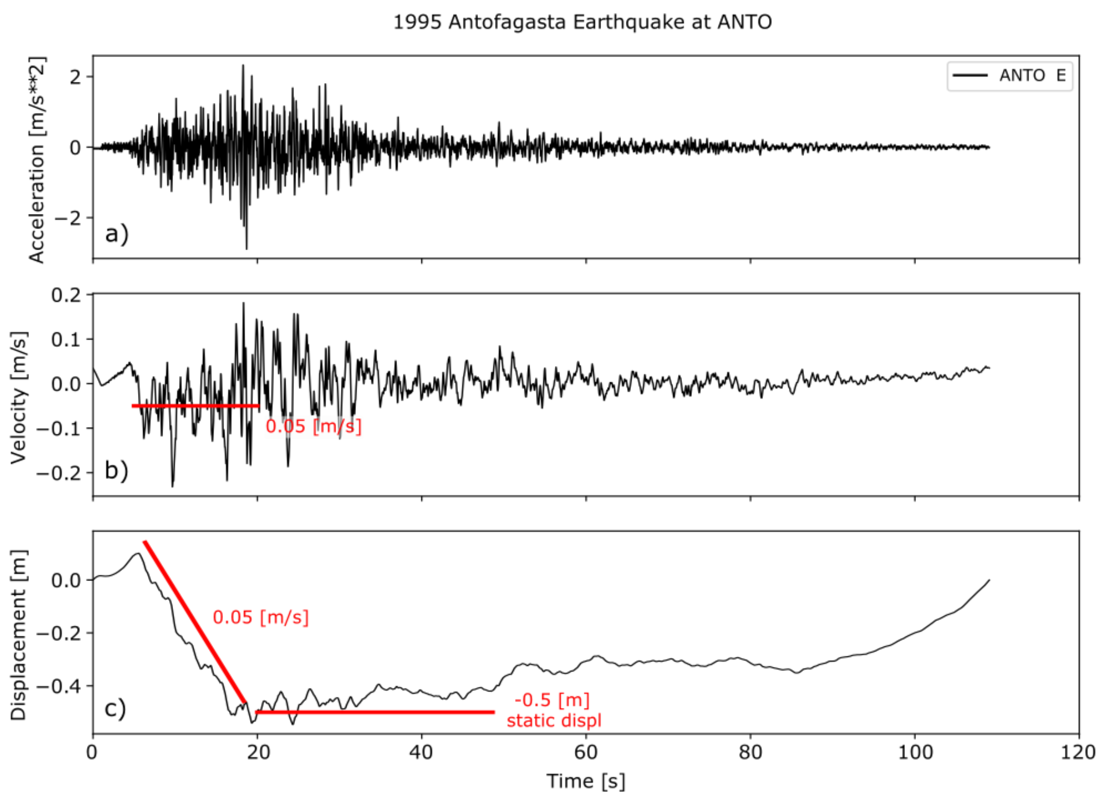

Figure 2. a) Strong-motion record for the east-west component from the ANTO station for the Antofagasta earthquake (M_w8.0) of July 31, 1995. **b)** Integrated strong-motion record from the ANTO station using the Boore (2001) methodology. **c)** Doubly integrated strong-motion record from the ANTO station. Red line shows the static displacement and the ground-velocity drop during the main arrival at this station.

A multitaper algorithm was used in conjunction with the DFT (Discrete Fourier Transform) to ensure that the spectrum is well estimated across most of the frequency band, avoiding loss of information when calculating the spectrum (Park et al., 1987; Prieto et al., 2009). Finally, a smoothing filter was applied to remove oscillations in the spectrum (Konno and Ohmachi, 1998). We did not correct the velocity spectra for attenuation because there is no general model of the distribution of Q-value in Chile. As observed in the acceleration spectrum of Figure 3, the acceleration spectrum is flat up to at least 7 Hz, but this needs further work. Attenuation has been studied in Chile in some areas (e.g., Schurr and Rietbrock (2004), Lancieri et al. (2012), and Neighbors et al. (2015)). These studies found kappa values in the order of 0.03 which agrees with the above estimate for the cut-off frequency (6.6 Hz).

As discussed by Madariaga et al. (2019) the well-known problem with the double-integration of accelerograms can be reduced using the velocity records to compute the spectrum. When available these ground-velocity spectra records were compared with once-differentiated displacement records of the GNSS signal (Melgar et al., 2013; Baez et al., 2018). We are aware that integrating the accelerograms once to velocity, produces weak low-frequency noise that could affect the actual estimation of the spectrum. For this reason, we computed the velocity spectrum by dividing the acceleration spectrum by $i\omega$ to avoid the use of filters that may affect the spectral estimation (Figure 3).

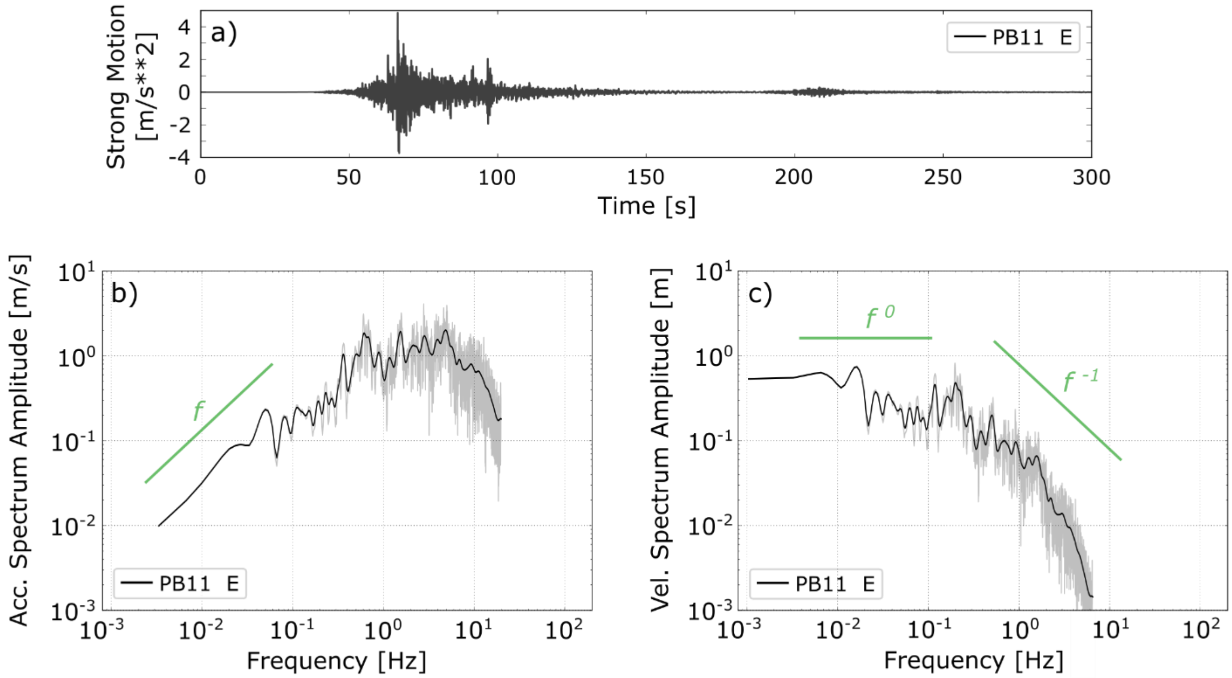

195

196 **Figure 3. a)** East-west component for the PB11 station acceleration record for the April 1st
197 earthquake in Iquique (M_w8.2). **b)** Acceleration spectrum obtained directly from the record. **c)**
198 Velocity spectrum obtained from the integrated acceleration spectrum. Both spectra have a Konno-
199 Ohmachi plotted with a black continuous line.

200

201 **3.1 Ground-velocity spectral model**

202 The ground-motion produced by a shallow thrust earthquake can be quite complex as
203 shown by numerical simulations. For a simple double couple source embedded in a half-space, the
204 static-field is well known, but at intermediate frequencies (when the wavelength is comparable to
205 the size of the source and the distance), the dynamic wavefield can only be computed using
206 numerical methods that take into account the presence of the free surface and shallow structure.
207 For a simple half-space, near-field velocities can be computed using the expressions derived by
208 Johnson (1964), but they are difficult to compute. The main effect of the free surface is to produce
209 strong surface waves that have no closed-form expressions. The Rayleigh waves follow
210 immediately after the shear wave and dominate the intermediate wavefield. At higher frequencies,
211 the spectrum is usually modeled using the Brune (1970) far-field equations.

In the following, we will compare the broad-band velocity spectra computed from accelerometers with the model proposed by Brune (1970) for the radiation from a circular source. In this model, the velocity spectrum has the following shape as a function of frequency f

$$\dot{u}(f) = 2\pi f \frac{\Omega_0}{1 + \left(\frac{f}{f_c}\right)^2} \ , \tag{1}$$

where at low frequencies the spectrum has an asymptote (Ω_0), a corner frequency f_c and a high-frequency decay as an inverse frequency f. In this case, we must estimate the values of Ω_0 and f_c for our theoretical model.

The stress drop $\Delta\sigma$ can be calculated from the seismic moment M_0 and the radius of the source r, according to Eshelby (1957) as

$$\Delta\sigma = \frac{7}{16}\left(\frac{M_0}{r^3}\right) \ , \tag{2}$$

Brune (1970) relates the corner frequency to the source radius as

$$f_c = k\frac{\beta}{r} \ , \tag{3}$$

where β is the shear wave velocity. k is a constant parameter that depends on the specific theoretical model. Here we will assume $k = 0.32$ as proposed by Madariaga (1976) for circular crack with a rupture velocity of 90% of the shear wave velocity. Therefore,

$$f_c = 0.32\frac{\beta}{r} . \tag{4}$$

Combining (2) and (4) we finally obtain that

$$\Delta\sigma = M_0\left(\frac{f_c}{0.42\beta}\right)^3 . \tag{5}$$

We estimate the theoretical corner frequency for each event assuming a constant $\Delta\sigma$ ($\Delta\sigma = 10$ MPa) and a value of M_0 obtained from the earthquake magnitude using the expression

$$M_w = \frac{3}{2}(log_{10}M_0 - 9.1) . \tag{6}$$

Finally, we calculate Ω_0 from M_0 as

$$M_0 = \frac{4\pi\rho R\beta^3}{F\langle R\rangle}\Omega_0\,, \tag{7}$$

where ρ is the density of the medium close to the source, R is the distance from the source to the station, F is the effect of the free surface and $\langle R\rangle$ is the average radiation pattern. In this case, we assume $F = 2$ and $\langle R\rangle = 0.67$.

The peak of the equation (1) is at

$$\dot{u}_{max} = \pi\, f_c\Omega_0 \propto M_0^{2/3} \tag{8}$$

Since from (5) $f_c \propto M_0^{-1/3}$ for a given stress drop.

Let us now consider the near-field; as shown by Aki and Richards (2002) the velocity-field generated by a double couple source of moment $M_0(t)$ buried in an elastic medium can be approximated by the S wave as

$$\dot{u}_{NF}(r,t) \cong \frac{1}{4\pi\rho\beta^2}\frac{C^{NF}}{r^2}\dot{M}_0\left(t-\frac{r}{\beta}\right), \tag{9}$$

where C_{NF} is the near-field radiation pattern defined by Aki and Richards (2002). This expression is valid at low frequencies because it does not take into account the interaction of seismic waves with the free surface. Transforming to the frequency domain, the near-field at low frequencies approaches

$$\dot{u}(r,\omega) = \frac{1}{4\pi\rho\beta^2}\frac{C^{NF}}{r^2}\dot{M}_0(\omega). \tag{10}$$

This expression is remarkably like the far-field displacement spectrum from a point double couple except for the near-field radiation pattern and the inverse square dependency on distance *r*. The limit of the amplitude of the velocity spectra $\tilde{\dot{u}}(\omega)$ at low frequencies is the static displacement. As derived by Madariaga et al. (2019)

$$\lim_{\omega\to 0}\tilde{\dot{u}}(\omega) = \int_{-\infty}^{\infty}\dot{u}(t)dt = u(\infty)\,, \tag{11}$$

where $u(\infty)$ is the static displacement at the station. The relation (11) between permanent ground-displacement and the low-frequency trend of the ground-velocity spectrum was used by Rupakhety et al. (2010), and Inbal and Ziv (2020) to correct for the displacement jump or "fling" observed in ground-displacement at close distances from the source. We do not make those corrections here because we are interested mainly in the spectral properties of accelerograms.

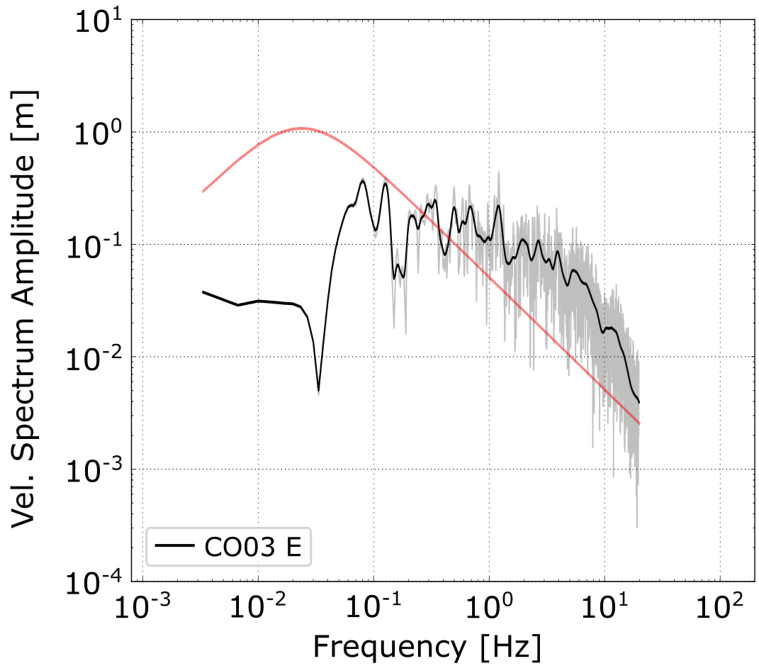

Figure 4. Velocity spectrum of the east-west component from CO03 station for the event of September 16, 2015, at Illapel (M_w8.3). The observed spectrum is shown in grey on which we superimpose the spectrum smoothed with a Konno-Ohmachi filter plotted with a continuous black line. The velocity spectrum model by Brune (1970) computed using eq. (8) is shown in red.

In Figure 4 we show the velocity spectrum computed at station CO03 for the Illapel earthquake of September 16, 2015. It has a flat trend at intermediate to low frequencies, quite unlike the theoretical Brune spectrum plotted in red. The near-field does not only affect low frequencies but a broad spectral range.

4. Comparison between continuous GPS and accelerometer spectra

We compare the velocity spectra computed from strong-motion and cGNSS time series. The strong-motion records were integrated in the frequency domain as explained earlier and the cGNSS were numerically differentiated. We used the GPS kinematic records processed by Baez et al. (2018) and by Ruhl et al. (2019). We compare the velocity spectra obtained from the acceleration and displacement records in Figure 5. We observe a very good agreement between both spectra at low frequencies up to approximately 0.2 Hz, which agrees with several authors (Emore et al., 2007; Bock et al., 2011) who found a good coincidence between both signals in the time domain. This similarity can be observed in the two horizontal components of the recordings, despite poorer resolution of the vertical displacement component record of cGNSS (Figures S1-S8).

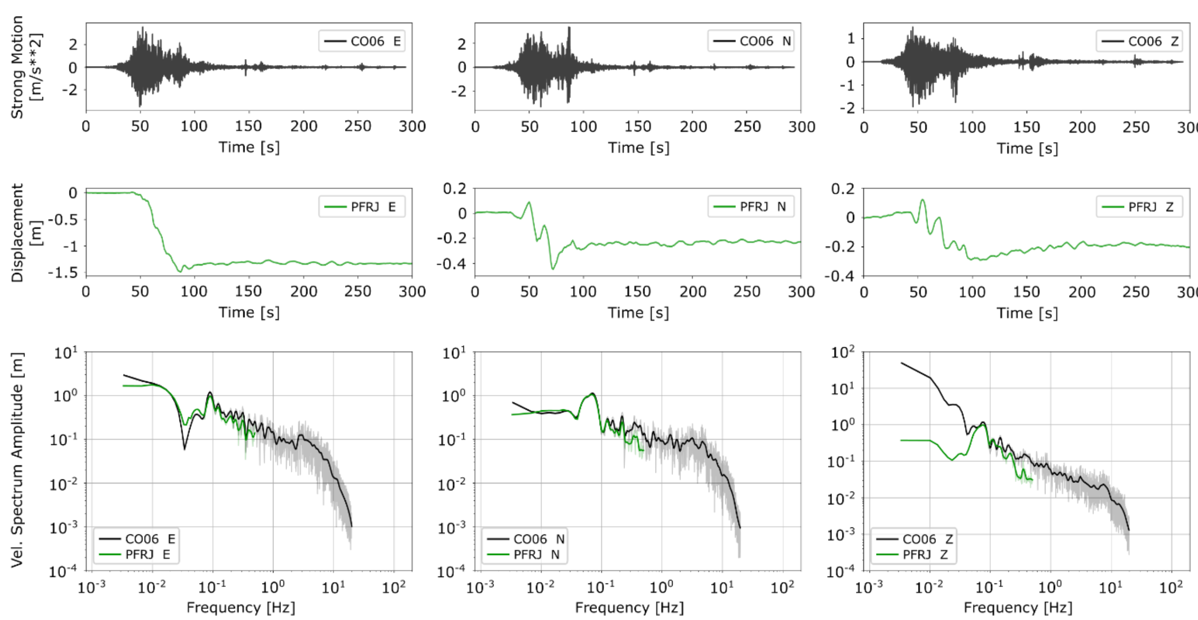

Figure 5. a) Three components of the acceleration records obtained at the CO06 station of the CSN network for the 16 September 2016 Illapel earthquake. **b)** GNSS displacement at station PFRJ, collocated with the CO06 accelerometer. **c)** Velocity spectrum computed from the acceleration record (black) and from the displacement record (green). Both spectra were smoothed with a Konno-Ohmachi filter.

As predicted by eq. (11), a flat velocity spectral trend is observed at low frequencies both in the cGNSS spectrum as well as in the velocity spectrum computed from strong ground records. This means that these records are dominated by the near-field and surface waves. Figures 6, 7, and 8 show the integrated acceleration spectra and the differentiated displacement spectra of the closest available stations for four earthquakes: Iquique 2014 (PSGCX) along with its main aftershock (TA01), Illapel 2015 (CO06), Chiloé 2016 (GO07) and Maule 2010 (CCSP and ROC1). Each of these earthquakes produced significant static displacements at the sites, as can be seen in the GNSS records. Depending on the earthquake, the displacements vary from some centimeters to hundreds of centimeters, for instance, the CO06 station for the 2015 Illapel earthquake has a displacement of ~140 cm, and CCSP for the Maule earthquake had a displacement of ~300 cm, both in their East-West components.

An excellent agreement can be observed between the static displacement observed from the GNSS record and the low-velocity spectral amplitude in both records. This confirms the relation (11) between the low-frequency asymptote of velocity spectra with the static displacement derived from GNSS records. However, possible effects on the integrated acceleration spectrum are evident at the low-frequency limit and are corrected by the differentiated displacement spectrum. As expected, GNSS data is much more robust at low frequencies than accelerograms. Madariaga et al. (2019) had already shown this relationship for the 1 April 2014 event in Iquique, where it is possible to determine, from the velocity spectrum, the static displacement produced by the earthquake at the PB11 station.

The spectra of these recent large Chilean earthquakes recorded close to their source (Figures 6, 7, 8, and Figures S1-S8) show a constant low-frequency trend in velocity at low frequencies and decay as f^{-1} at high frequencies. The dashed horizontal line in the low-frequency end of the spectra shows the static displacement observed at the collocated GNSS station. We observe that for all these records, the velocity spectrum derived from accelerograms and GNSS records are the same, except for the recording of the Maule earthquake in Concepción (CCSP) in Figure 8. At this site, the ground-displacement was 300 cm, so that the strong-motion at this site is probably affected by inaccurate recording of low frequencies. Unfortunately, we do not have any other records of the Maule earthquake in the near-field to evaluate the accuracy of velocities determined from strong-motion integration.

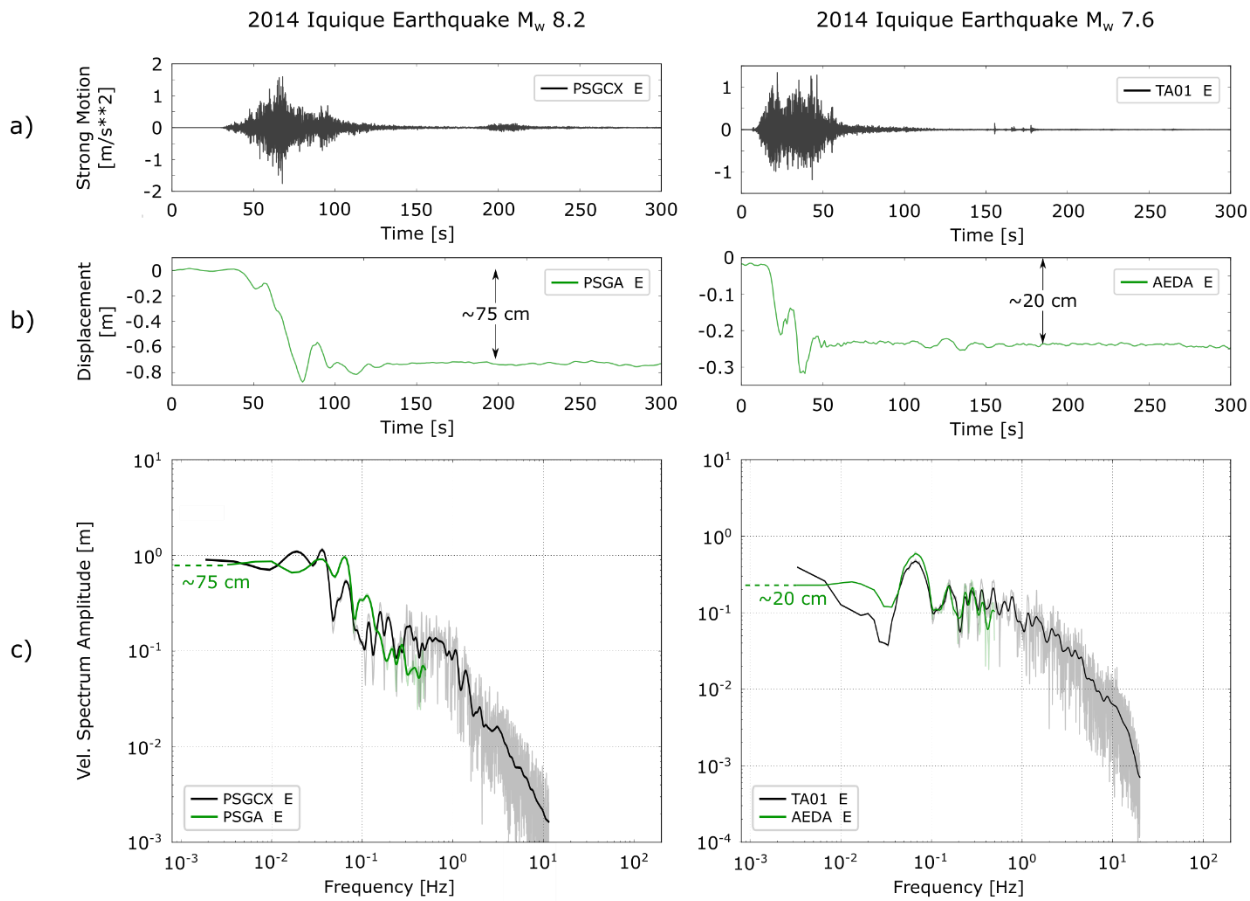

Figure 6. a) Acceleration record for the east-west component of the PSGCX station that recorded the magnitude M_w 8.2 Iquique earthquake of 1 April 2014 (left column) and for the TA01 station that recorded the Iquique aftershock of magnitude M_w 7.6 on 3 April 2014 (right column). **b)** GNSS displacement recording for the east-west component of the PSGA station that recorded the magnitude M_w 8.2 Iquique earthquake of 1 April 2014 (left column) and for the AEDA station that recorded the Iquique aftershock of magnitude M_w 7.6 on 3 April 2014 (right column). **c)** Velocity spectra obtained from both earthquakes, integrated acceleration (black) and differentiated displacement (green). The dashed horizontal lines at low-frequency show the excellent fit between low-frequency trend of the velocity spectra and the static ground-displacement derived from GNSS records.

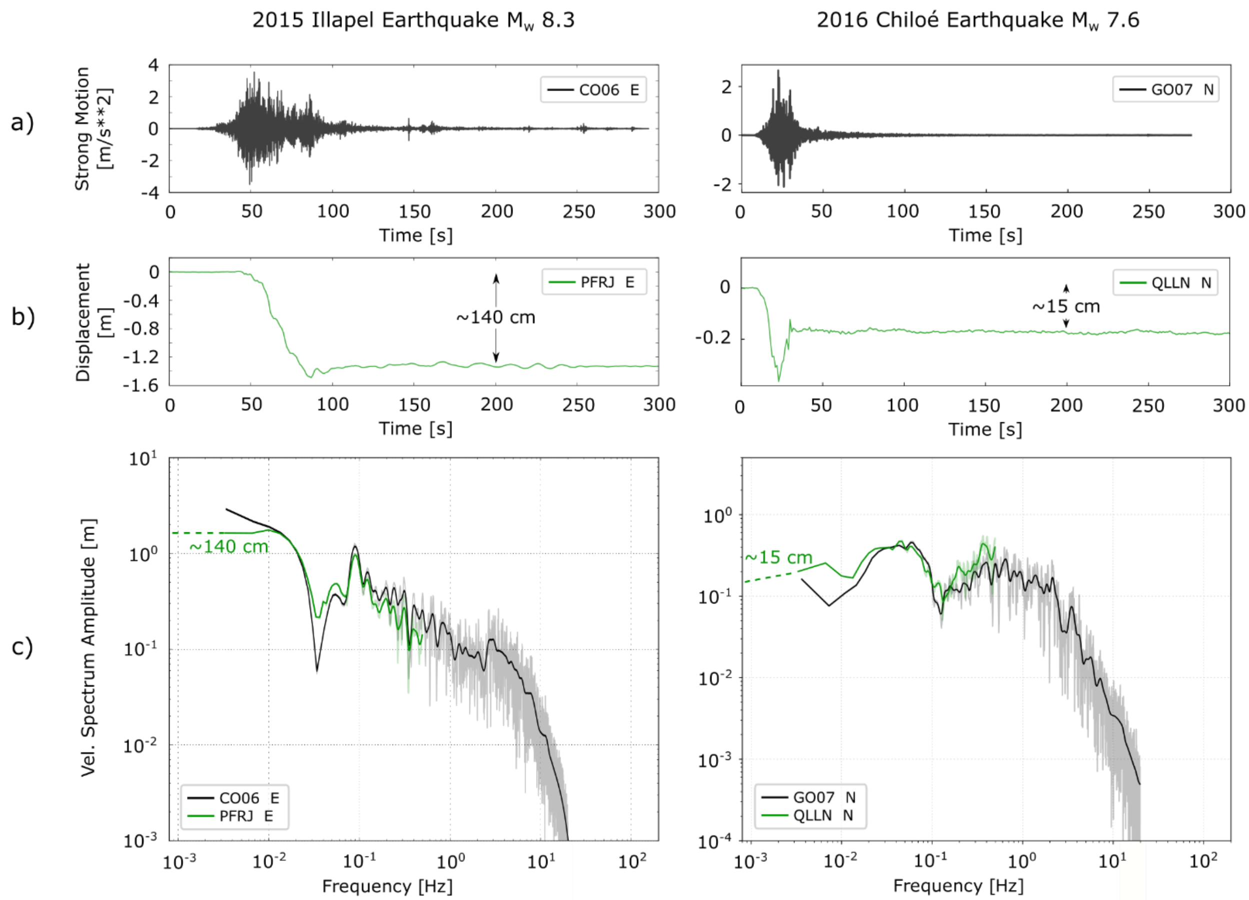

Figure 7. a) Acceleration record for the east-west component recorded at station CO06 for the 15 September 2015 Illapel earthquake of magnitude M_w 8.3 (left column) and for the GO07 station that recorded the Chiloé earthquake of magnitude M_w 7.6 on 25 December 2016 (right column). **b)** GNSS displacement record for the east-west component recorded at station PFRJ for the 15 September 2015 Illapel earthquake of magnitude M_w 8.3 (left column) and for station QLLN recording of the 25 December 2016 event in Chiloé of magnitude M_w 7.6 (right column). **c)** Velocity spectra obtained from both records, integrated acceleration (black) and differentiated displacement (green). The dashed horizontal lines at low-frequency show the excellent fit between low-frequency trend of the velocity spectra and the static ground-displacement derived from GNSS records.

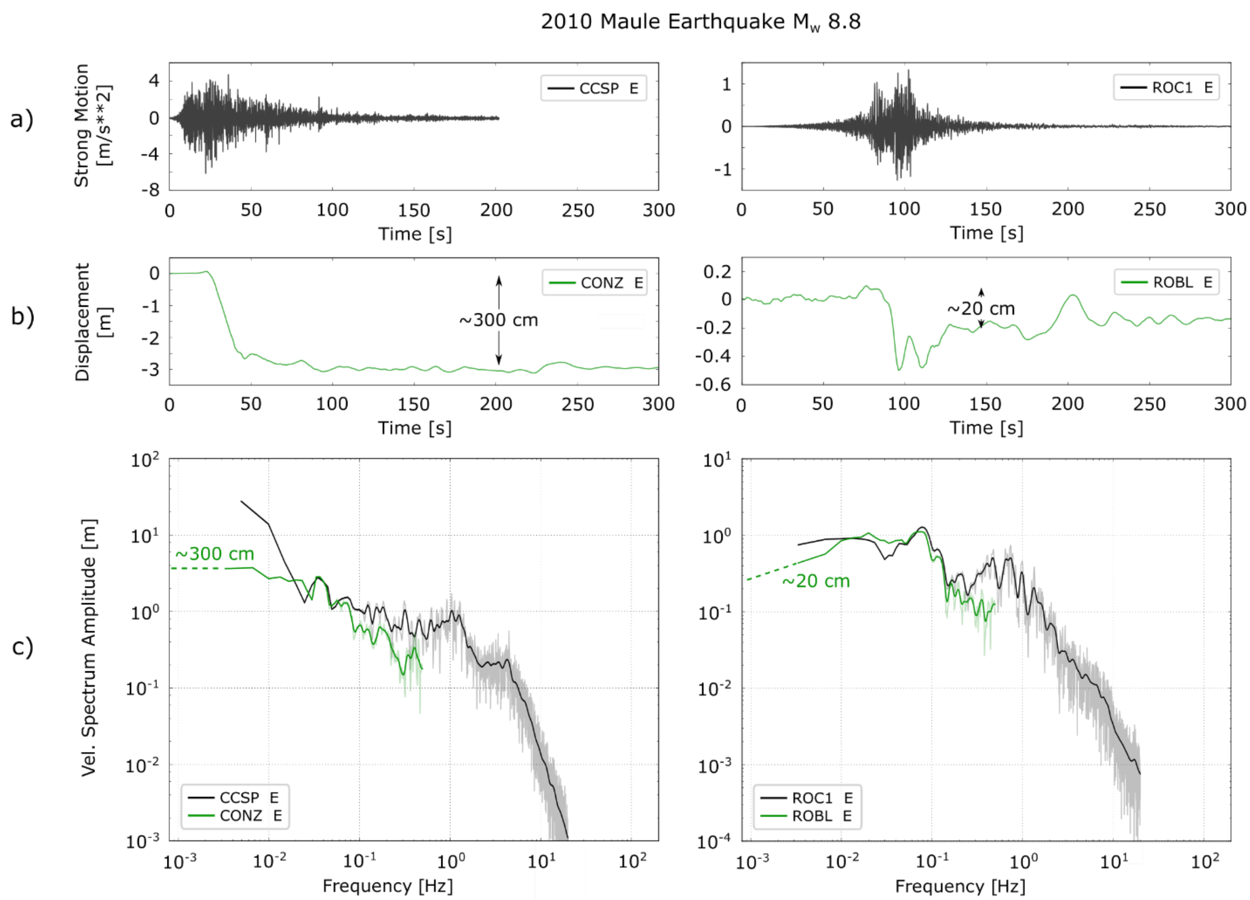

Figure 8. a) Acceleration records for the east-west component of the CCSP and ROC1 strong-motion recordings of the 27 February 2010, M_w 8.8 megathrust earthquake. **b)** GNSS displacement records for the east-west component of the CONZ and ROBL GNSS recording of the 27 February 2010, M_w 8.8 megathrust earthquake. **c)** Velocity spectra obtained from both records, by integrating acceleration in the spectral domain (black) and differentiating GNSS displacement (green). The CCSP station is located near Concepción in the neighborhood of the main fault, while ROC1 is situated close to 400 km North of the hypocenter. The dashed horizontal lines at low-frequency in the near-field record of station ROC1 shows an excellent fit between velocity spectra and static ground-displacement. The low-frequency spectrum at station CCSP is not flat indicating that the integration of the strong-motion record is not accurate for frequencies bellow 0.02 Hz (50 s period).

5. Influence of magnitude and distance in the earthquake spectra

Several authors have documented changes in the shape of the displacement, velocity, or acceleration spectrum, both in the near- and far-fields (Boatwright and Choy, 1989; Archuleta et al., 2016; Denolle and Shearer, 2016; Madariaga et al., 2019). Here we show the transition from f^{-1} to f^{-2} as a function of distance from the source and magnitude of the events.

5.1 Spectrum of earthquakes with different magnitude

We considered events with different magnitudes but observed at a similar hypocentral distance close to 90 km. Figure 9 shows the behavior of the velocity spectrum as a function of magnitude. It is evident that in the transition from an event of magnitude M_w 6.5 to an M_w 5.6 event, the velocity spectra for the smaller magnitude events decay to zero at low frequencies. The corner frequency of the earthquake becomes evident for the smaller and the spectra are similar to that proposed by Brune (1970). For larger magnitudes, on the other hand, the corner frequency becomes increasingly difficult to define. For the largest events, the M_w 8.2, 2014 Iquique earthquake, the velocity spectrum is flat at low frequencies and reaches a value of 1 meter.

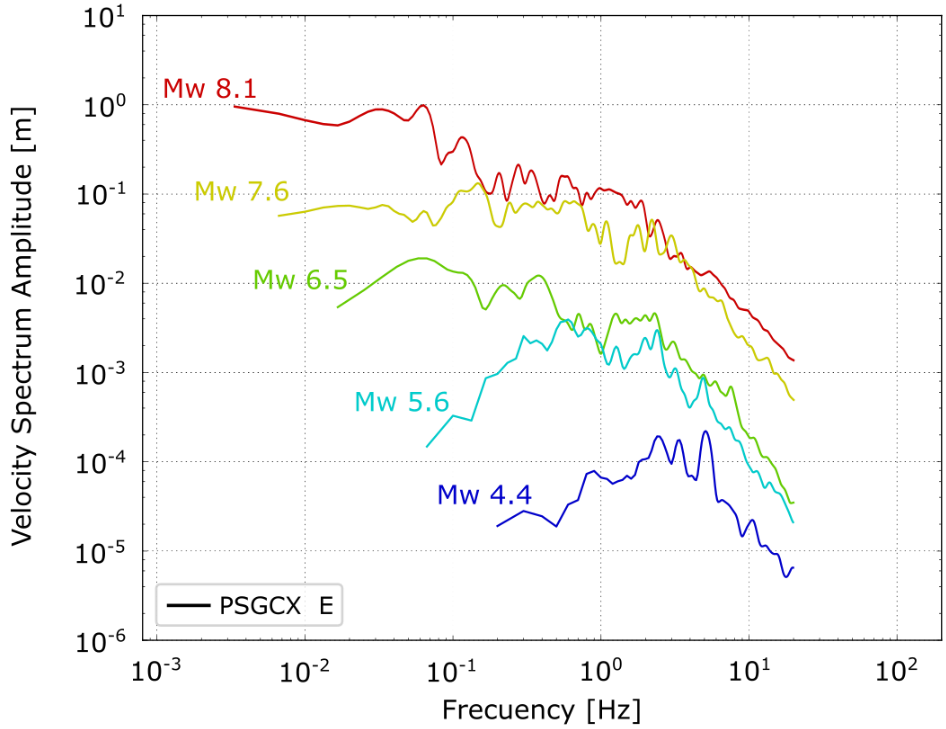

Figure 9. Velocity spectrum for events of different magnitude recorded for the east-west component of the PSGCX station in northern Chile. The events have a relatively similar hypocentral distance to the station. The earthquake information of these events is shown in Table S3.

5.2 Spectra of a large earthquake at different observation distances

The static displacement decreases with distance from the source as r^{-2} in contrast to the amplitude of far-field seismic waves that decrease as r^{-1}, considering an isotropic and homogeneous medium.

Figure 10 shows four velocity spectra recorded at four stations for the Iquique earthquake of M_w 8.2. In this figure, we observe that the two closest stations PSGCX and PB08, both at less than 200 km from the source have a flat velocity spectrum at low frequencies. However, there is a sudden change of slope in the low frequencies for the farther stations PB05 located at a distance of approximately 370 km and PB10 at 437 km. Madariaga et al. (2019) estimate that the far-field becomes dominant over the near-field beyond distances of 400 km assuming an average P-wave velocity of 6 km/s and a P/S velocity ratio of 1.73.

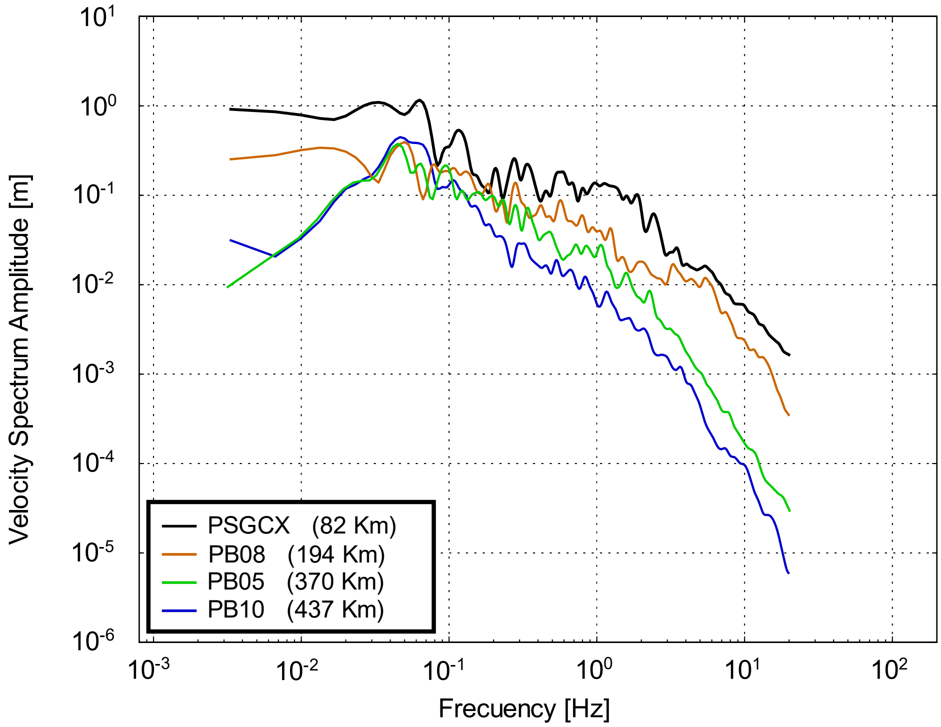

Figure 10. Velocity spectrum for the east-west component of four stations that recorded the April 1, 2014 earthquake ordered as a function of hypocentral distance. Clearly the spectral shape changes for distances greater than 194 Km. The peak in the velocity spectra of stations PB05 and PB10 is the corner frequency for this event.

6. Discussion

We have studied the velocity spectra of the 8 largest recent earthquakes in Chile. These records significantly increase the available spectra for Chilean earthquakes that are needed to produce reliable strong-motion prediction for future earthquakes. Due to the limited number of strong-motion records available in Chile, seismic spectra have been estimated by assuming that the typical earthquake spectrum is that proposed by Brune (1970). As discussed by Madariaga et al. (2019) strong ground-motion spectra contain both far-field and near-field terms as well as surface wave components.

Both the velocity spectra derived from strong-motion and cGNSS records are significantly different from the usual far-field model of Brune (1970). The velocity spectra of large magnitude earthquakes show a clear flat low-frequency trend. The amplitude observed at low frequencies in the spectra is a measure of static co-seismic displacement produced by the earthquake at the location of the station. Although it is difficult to estimate low frequencies from acceleration spectra because of the well-known instability of velocity traces integrated from accelerograms, GNSS is a good complement in the frequency band needed to estimate its amplitude. In the velocity spectra shown in Figures 6, 7, and 8 we cannot determine a clear corner frequency of the earthquakes: the velocity spectra do not have a clear decay up to about 1 Hz where an abrupt decay begins. It is highly likely that this strong decay, which is different for each spectrum, could be related to scattering and attenuation effects that occur at high frequencies.

The effect of the near-field on the velocity spectrum is to produce a flat trend at low frequencies (Madariaga et al., 2019) that prevents the observation of the corner frequency. We understand then that when the near-field dominates strong-motion, the Brune spectrum cannot be observed. The question is for which distance and type of earthquakes do we observe the Brune spectrum? The magnitude of the earthquake may give us some clues about this. The smaller the magnitude of the event, the smaller the co-seismic displacement so that the velocity spectrum at low frequencies will converge to zero, producing the characteristic Brune spectrum with an evident corner frequency. Figure 9 shows that for earthquakes recorded at a similar distance (~90 Km) from the source (see Table S3), there is a transition magnitude at which the spectrum begins to decay in amplitude at low frequencies. In the case of Figure 9, for earthquakes with magnitudes between $M_w 5.6 - 6.5$ it is possible to observe a change in the low frequencies that suggests the transition from a Brune model to a spectrum dominated by the near-field.

Boatwright and Choy (1989) were among the first authors to highlight the differences between the acceleration spectrum of moderate and large earthquakes. Removing the near-source free surface effect in far-field accelerograms, they made a distinction in the shape of the strong-motion spectrum for earthquakes with a seismic moment $M_0 < 10^{20}$ [N m], which has an increase of f^2 at low frequencies, and those of seismic moment $M_0 > 10^{20}$ that have an intermediate frequency of $f^{5/4}$. These results show a break in the scaling law for moderate and large magnitude earthquakes, concluding that a large earthquake cannot be obtained by scaling of the spectra of moderate events.

Figure 11 shows the relationship between the static displacement and the peak ground-displacement (PGD), and the seismic moment M_0 of the last seven major earthquakes. The PGD was obtained from relation (8) using accelerograms or, preferably, from high-rate GNNS records when they were available (see Table S4 for availability). The scaling relationship is proportional to $M_0^{2/3}$, which is similar to that proposed by Singh et al. (2020) who reported a break in the relationship between PGD and seismic momentum M_0 using seismometers, accelerometers, and cGPS records observed in the near-field in the Mexican subduction zone. They proposed that PGD scaled like $M_0^{2/3}$ for events of magnitude $M_w \leq 6$; while it scaled like $M_0^{1/3}$ for events of magnitude $M_w \geq 8$. This is not the case for large Chilean earthquakes that rupture to the trench and then propagate bilaterally along the coast. We definitely need more data before we can conclude about scaling of PGD in the near-field. Also, we show that for large earthquakes, like those studied here, the static displacement is a good approximation to the PGD (Ruhl et al., 2019).

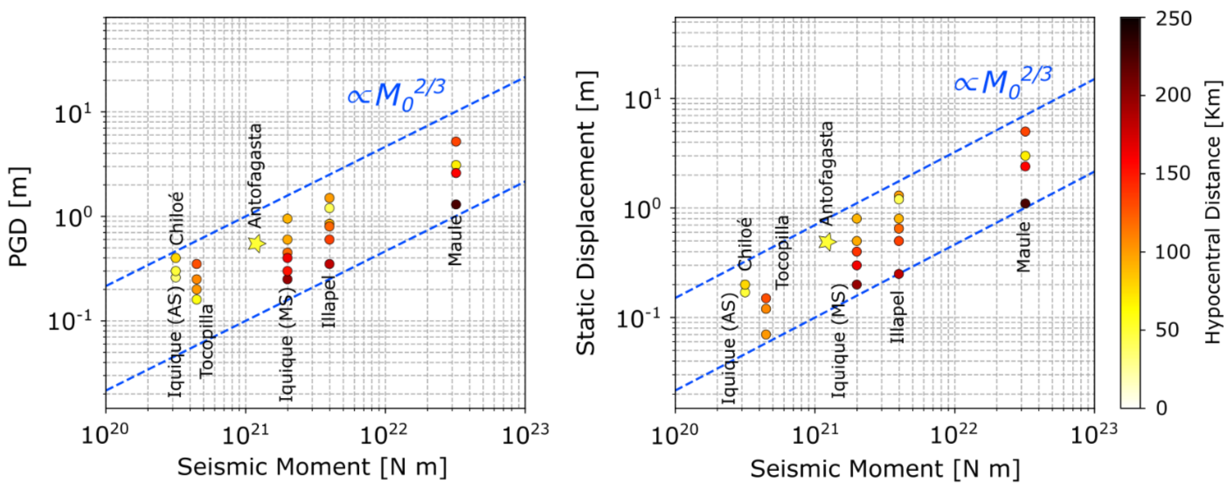

Figure 11. PGD as a function of seismic moment M_0 for the last 7 large thrust earthquakes in Chile. With discontinuous blue lines, the ratio PGD $\propto M_0^{2/3}$ is shown and with color scale the source station distance of the GNSS record used. The PGD and static displacement for the Antofagasta earthquake is computed using the double-integrated acceleration register (star). The PGD and static displacement values are listed on Table S4.

From the previous discussion, it is obvious that hypocentral distance plays a key role in the spectral shape of large earthquakes. Madariaga et al. (2019) made a rough approximation that Brune's far-field spectrum should be observed at distances larger than 400 Km. Figure 10 shows a clear transition between the spectra at the PB08 station at a distance of 194 km and that at the PB05 station at a distance of 370 Km. We do not have spectra at intermediate distances to determine more accurately when the near-field becomes negligible with respect to the far-field.

We believe that both distance and magnitude determine the region where near- and far-field spectra are dominant. However, we would like to emphasize the importance of the effect of the near-field and its influence on the calculation of the spectrum of an earthquake. Previous studies had already observed a similar decay in the displacement spectrum, attributing it to a modification of the Brune model due to a double corner frequency or modifications of the far-field waves (Archuleta et al., 2016; Denolle and Shearer, 2016).

Future studies of the near-field spectra will require rethinking several aspects: (1) The analysis of the static and dynamic parameters of the seismic source, with which the scaling laws are proposed, could vary for large earthquakes in which the near-field dominates so that the Brune spectral model cannot be assumed to be valid, (2) Regarding strong-motion prediction studies, in which the Brune's model is also assumed, they should be reviewed considering the spectral properties of large earthquakes.

7. Conclusions

We show the strong influence of the near-field in the velocity spectrum of all the large earthquake of $M_w > 7.5$ recorded in Chile. We observe that all of the velocity spectra become flat at low frequencies and close distances, and the velocity spectral level converges to the static co-seismic displacement of the earthquake. This is quite different from the classical far-field spectral models proposed by Aki (1967) and Brune (1970). It is difficult to quantify the transition distance and magnitude because we have limited data for the moment. Both criteria are currently not considered when studying spectral parameters or strong-motion prediction in earthquake engineering and would change the modeling of the strong-motion for large earthquakes. Finally, we observe that peak ground-displacement and the static GNSS displacement scales like moment to the power 2/3 up to the largest event observed in Chile (M_w 8.8, Maule 2010).

Acknowledgements

The authors thank to Editor Dr. Eiichi Fukuyama and anonymous reviewers for their constructive remarks that improved our manuscript. This study was supported by FONDECYT contract N° 1170430 and by PRS (Programa de Riesgo Sísmico of Universidad de Chile). The acceleration and GNSS data used in this study was made available by the Centro Sismológico Nacional of the University of Chile (CSN). It can be retrieved from their web page. We thank the Civil engineering department of the University of Chile for the data for the 1995 Antofagasta and 2005 Tarapacá earthquakes.

References

Abercrombie, R. E. (1995). Earthquake source scaling relationships from− 1 to 5 ML using seismograms recorded at 2.5-km depth. *Journal of Geophysical Research: Solid Earth*, *100*(B12), 24015-24036.

Aki, K. (1967). Scaling law of seismic spectrum. *Journal of Geophysical Research*, *72*(4), 1217-1231.

Allmann, B. P., & Shearer, P. M. (2007). Spatial and temporal stress drop variations in small earthquakes near Parkfield, California. *Journal of Geophysical Research: Solid Earth*, *112*(B4).

Archuleta, R. J., & Ji, C. (2016). Moment rate scaling for earthquakes 3.3≤ M≤ 5.3 with implications for stress drop. *Geophysical Research Letters*, *43*(23), 12-004.

Baez, J. C., Leyton, F., Troncoso, C., del Campo, F., Bevis, M., Vigny, C., Moreno, M., Simons, M., Kendrick, E., Parra, H., & Blume, F. (2018). The Chilean GNSS network: Current status and progress toward early warning applications. *Seismological Research Letters*, *89*(4), 1546-1554.

Boatwright, J., & Choy, G. L. (1989). Acceleration spectra for subduction zone earthquakes. *Journal of Geophysical Research: Solid Earth*, *94*(B11), 15541-15553.

Bock, Y., Prawirodirdjo, L., & Melbourne, T. I. (2004). Detection of arbitrarily large dynamic ground motions with a dense high-rate GPS network. *Geophysical Research Letters*, *31*(6).

Bock, Y., Melgar, D., & Crowell, B. W. (2011). Real-time strong-motion broadband displacements from collocated GPS and accelerometers. *Bulletin of the Seismological Society of America*, *101*(6), 2904-2925.

Boore, D. M. (2001). Effect of baseline corrections on displacements and response spectra for several recordings of the 1999 Chi-Chi, Taiwan, earthquake. *Bulletin of the Seismological Society of America*, *91*(5), 1199-1211.

Boroschek, R. L., Contreras, V., Kwak, D. Y., & Stewart, J. P. (2012). Strong ground motion attributes of the 2010 Mw 8.8 Maule, Chile, earthquake. *Earthquake Spectra*, *28*(S1), S19-S38.

Brune, J. N. (1970). Tectonic stress and the spectra of seismic shear waves from earthquakes. *Journal of geophysical research*, *75*(26), 4997-5009.

Cesca, S., Grigoli, F., Heimann, S., Dahm, T., Kriegerowski, M., Sobiesiak, M., Tassara, C & Olcay, M. (2016). The Mw 8.1 2014 Iquique, Chile, seismic sequence: a tale of foreshocks and aftershocks. *Geophysical Journal International*, *204*(3), 1766-1780.

Chlieh, M., De Chabalier, J. B., Ruegg, J. C., Armijo, R., Dmowska, R., Campos, J., & Feigl, K. L. (2004). Crustal deformation and fault slip during the seismic cycle in the North Chile subduction zone, from GPS and InSAR observations. *Geophysical Journal International*, *158*(2), 695-711.

Delouis, B., Monfret, T., Dorbath, L., Pardo, M., Rivera, L., Comte, D., ... & Cisternas, A. (1997). The Mw= 8.0 Antofagasta (northern Chile) earthquake of 30 July 1995: A precursor to the end of the large 1877 gap. *Bulletin of the Seismological Society of America*, *87*(2), 427-445.

Delouis, B., & Legrand, D. (2007). Mw 7.8 Tarapaca intermediate depth earthquake of 13 June 2005 (northern Chile): Fault plane identification and slip distribution by waveform inversion. *Geophysical Research Letters*, *34*(1).

Delouis, B., Pardo, M., Legrand, D., & Monfret, T. (2009). The M w 7.7 Tocopilla earthquake of 14 November 2007 at the southern edge of the northern Chile seismic gap: Rupture in the deep part of the coupled plate interface. *Bulletin of the Seismological Society of America*, *99*(1), 87-94.

Delouis, B., Nocquet, J. M., & Vallée, M. (2010). Slip distribution of the February 27, 2010 Mw= 8.8 Maule earthquake, central Chile, from static and high-rate GPS, InSAR, and broadband teleseismic data. *Geophysical Research Letters*, *37*(17).

Denolle, M. A., & Shearer, P. M. (2016). New perspectives on self-similarity for shallow thrust earthquakes. *Journal of Geophysical Research: Solid Earth*, *121*(9), 6533-6565.

Duputel, Z., Jiang, J., Jolivet, R., Simons, M., Rivera, L., Ampuero, J. P., Riel B., Owen, S. E., Moore, A. W., Samsonov, S. V. Ortega Culaciati, F. & Minson, S. E. (2015). The Iquique earthquake sequence of April 2014: Bayesian modeling accounting for prediction uncertainty. *Geophysical Research Letters*, *42*(19), 7949-7957.

Elósegui, P., Davis, J. L., Oberlander, D., Baena, R., & Ekström, G. (2006). Accuracy of high-rate GPS for seismology. *Geophysical Research Letters*, *33*(11).

Emore, G. L., Haase, J. S., Choi, K., Larson, K. M., & Yamagiwa, A. (2007). Recovering seismic displacements through combined use of 1-Hz GPS and strong-motion accelerometers. *Bulletin of the Seismological Society of America*, *97*(2), 357-378.

Eshelby, J. D. (1957). The determination of the elastic field of an ellipsoidal inclusion, and related problems. *Proceedings of the royal society of London. Series A. Mathematical and physical sciences*, *241*(1226), 376-396.

Fuenzalida, A., Schurr, B., Lancieri, M., Sobiesiak, M., & Madariaga, R. (2013). High-resolution relocation and mechanism of aftershocks of the 2007 Tocopilla (Chile) earthquake. *Geophysical Journal International*, *194*(2), 1216-1228.

Inbal, A., & Ziv, A. (2020). Automatic Extraction of Permanent Ground Offset from Near-Field Accelerograms: Algorithm, Validation, and Application to the 2004 Parkfield Earthquake. *Bulletin of the Seismological Society of America*, *110*(6), 2638-2646.

IPOC (2006). GFZ German Research Centre For Geosciences & Institut Des Sciences De L'Univers-Centre National De La Recherche CNRS-INSU. IPOC seismic network. *Integrated Plate boundary Observatory Chile-IPOC. Other/Seismic Network*.

Ji, C., Larson, K. M., Tan, Y., Hudnut, K. W., & Choi, K. (2004). Slip history of the 2003 San Simeon earthquake constrained by combining 1-Hz GPS, strong motion, and teleseismic data. *Geophysical research letters*, *31*(17)

Johnson, L. R. (1974). Green's function for Lamb's problem. *Geophysical Journal International*, *37*(1), 99-131.

Kato, A., & Nakagawa, S. (2014). Multiple slow-slip events during a foreshock sequence of the 2014 Iquique, Chile Mw 8.1 earthquake. *Geophysical Research Letters*, *41*(15), 5420-5427.

Konno, K., & Ohmachi, T. (1998). Ground-motion characteristics estimated from spectral ratio between horizontal and vertical components of microtremor. *Bulletin of the Seismological Society of America*, *88*(1), 228-241.

Lancieri, M., Madariaga, R., & Bonilla, F. (2012). Spectral scaling of the aftershocks of the Tocopilla 2007 earthquake in northern Chile. *Geophysical Journal International*, *189*(1), 469-480.

Lange, D., Ruiz, J., Carrasco, S., & Manríquez, P. (2018). The Chiloé M w 7.6 earthquake of 2016 December 25 in Southern Chile and its relation to the M w 9.5 1960 Valdivia earthquake. *Geophysical Journal International*, *213*(1), 210-221.

Larson, K. M., Bodin, P., & Gomberg, J. (2003). Using 1-Hz GPS data to measure deformations caused by the Denali fault earthquake. *Science*, *300*(5624), 1421-1424.

Larson, K. M. (2009). GPS seismology. *Journal of Geodesy*, *83*(3-4), 227-233.

Lay, T., Ammon, C. J., Kanamori, H., Koper, K. D., Sufri, O., & Hutko, A. R. (2010). Teleseismic inversion for rupture process of the 27 February 2010 Chile (Mw 8.8) earthquake. *Geophysical Research Letters*, *37*(13).

León-Ríos, S., Ruiz, S., Maksymowicz, A., Leyton, F., Fuenzalida, A., & Madariaga, R. (2016). Diversity of the 2014 Iquique's foreshocks and aftershocks: clues about the complex rupture process of a Mw 8.1 earthquake. *Journal of Seismology*, *20*(4), 1059-1073.

Leyton, F., Leopold, A., Hurtado, G., Pastén, C., Ruiz, S., Montalva, G., & Saez, E. (2018). Geophysical characterization of the Chilean seismological stations: First results. *Seismological Research Letters*, *89*(2A), 519-525.

Madariaga, R. (1976). Dynamics of an expanding circular fault. *Bulletin of the Seismological Society of America*, *66*(3), 639-666.

Madariaga, R., Ruiz, S., Rivera, E., Leyton, F., & Baez, J. C. (2019). Near-field spectra of large earthquakes. *Pure and Applied Geophysics*, *176*(3), 983-1001.

Melgar, D., Bock, Y., Sanchez, D., & Crowell, B. W. (2013). On robust and reliable automated baseline corrections for strong motion seismology. *Journal of Geophysical Research: Solid Earth*, *118*(3), 1177-1187.

Melgar, D., Riquelme, S., Xu, X., Baez, J. C., Geng, J., & Moreno, M. (2017). The first since 1960: A large event in the Valdivia segment of the Chilean Subduction Zone, the 2016 M7. 6 Melinka earthquake. *Earth and Planetary Science Letters*, *474*, 68-75.

Moreno, M., Melnick, D., Rosenau, M., Baez, J., Klotz, J., Oncken, O., Tassara, A., Chen, J., Bataille, K., Bevis, M., Socquet, A., Bolte, J., Vigny, C., Brooks, B., Ryder, I., Grund, V., Smally, B., Carrizo, D., Bartsch, M. & Hase, H. (2012). Toward understanding tectonic control on the Mw 8.8 2010 Maule Chile earthquake. *Earth and Planetary Science Letters*, *321*, 152-165.

Neighbors, C., Liao, E. J., Cochran, E. S., Funning, G. J., Chung, A. I., Lawrence, J. F., Christensen, C., Miller, M., Belmonte, A., & Andrés Sepulveda, H. H. (2015). Investigation of the high-frequency attenuation parameter, κ (kappa), from aftershocks of the 2010 M w 8.8 Maule, Chile earthquake. *Geophysical Journal International*, *200*(1), 200-215.

Park, J., Lindberg, C. R., & Vernon III, F. L. (1987). Multitaper spectral analysis of high-frequency seismograms. *Journal of Geophysical Research: Solid Earth*, *92*(B12), 12675-12684.

Peyrat, S., & Favreau, P. (2010a). Kinematic and spontaneous rupture models of the 2005 Tarapacá intermediate depth earthquake. *Geophysical Journal International*, *181*(1), 369-381.

Peyrat, S., Madariaga, R., Buforn, E., Campos, J., Asch, G., & Vilotte, J. P. (2010b). Kinematic rupture process of the 2007 Tocopilla earthquake and its main aftershocks from teleseismic and strong-motion data. *Geophysical Journal International*, *182*(3), 1411-1430.

Prieto, G. A., Shearer, P. M., Vernon, F. L., & Kilb, D. (2004). Earthquake source scaling and self-similarity estimation from stacking P and S spectra. *Journal of Geophysical Research: Solid Earth*, *109*(B8).

Prieto, G. A., Parker, R. L., & Vernon III, F. L. (2009). A Fortran 90 library for multitaper spectrum analysis. *Computers & Geosciences*, *35*(8), 1701-1710.

Ruegg, J. C., Campos, J., Armijo, R., Barrientos, S., Briole, P., Thiele, R., Arancibia M., Cañuta J., Duquesnoy T., Chang M., Lazo, D., Lyon-Caen H., Ortlieb L., Rossignol J.C. & Serrurier L. (1996). The Mw= 8.1 Antofagasta (North Chile) earthquake of July 30, 1995: first results from teleseismic and geodetic data. *Geophysical Research Letters*, *23*(9), 917-920.

Ruhl, C. J., Melgar, D., Geng, J., Goldberg, D. E., Crowell, B. W., Allen, R. M., & Cabral-Cano, E. (2019). A global database of strong-motion displacement GNSS recordings and an example application to PGD scaling. *Seismological Research Letters*, *90*(1), 271-279.

Ruiz, S., Madariaga, R., Astroza, M., Saragoni, G. R., Lancieri, M., Vigny, C., & Campos, J. (2012). Short-period rupture process of the 2010 Mw 8.8 Maule earthquake in Chile. *Earthquake Spectra*, *28*(1_suppl1), 1-18.

Ruiz, S., Metois, M., Fuenzalida, A., Ruiz, J., Leyton, F., Grandin, R., Vigny, C., Madariaga, R., & Campos, J. (2014). Intense foreshocks and a slow slip event preceded the 2014 Iquique Mw 8.1 earthquake. *Science*, *345*(6201), 1165-1169.

Ruiz, S., Klein, E., del Campo, F., Rivera, E., Poli, P., Metois, M., Vigny, C., Baez, J. C., Vargas, G., Leyton, F., & Madariaga, R. (2016). The seismic sequence of the 16 September 2015 Mw 8.3 Illapel, Chile, earthquake. *Seismological Research Letters*, *87*(4), 789-799.

Ruiz, S., Moreno, M., Melnick, D., Del Campo, F., Poli, P., Baez, J. C., Leyton, F., & Madariaga, R. (2017). Reawakening of large earthquakes in south central Chile: The 2016 Mw 7.6 Chiloé event. *Geophysical Research Letters*, *44*(13), 6633-6640.

Ruiz, S., & Madariaga, R. (2018). Historical and recent large megathrust earthquakes in Chile. *Tectonophysics*, *733*, 37-56.

Rupakhety, R., Halldorsson, B., & Sigbjörnsson, R. (2010). Estimating coseismic deformations from near source strong motion records: methods and case studies. *Bulletin of Earthquake Engineering*, *8*(4), 787-811.

Schurr, B., & Rietbrock, A. (2004). Deep seismic structure of the Atacama basin, northern Chile. *Geophysical Research Letters*, *31*(12).

Schurr, B., Asch, G., Rosenau, M., Wang, R., Oncken, O., Barrientos, S., Salazar, P., & Vilotte, J. P. (2012). The 2007 M7. 7 Tocopilla northern Chile earthquake sequence: Implications for along-strike and downdip rupture segmentation and megathrust frictional behavior. *Journal of Geophysical Research: Solid Earth*, *117*(B5).

Schurr, B., Asch, G., Hainzl, S., Bedford, J., Hoechner, A., Palo, M., Wang, R., Moreno, M., Bartsch, M., Zhang, Y., Oncken, O., Tilmann, F., Dahm, T., Victor, P., Barrientos, S., & Vilotte J. P. (2014). Gradual unlocking of plate boundary controlled initiation of the 2014 Iquique earthquake. *Nature*, *512*(7514), 299-302.

Shearer, P. M., Prieto, G. A., & Hauksson, E. (2006). Comprehensive analysis of earthquake source spectra in southern California. *Journal of Geophysical Research: Solid Earth*, *111*(B6).

Singh, S. K., Pérez-Campos, X., Ordaz, M., Iglesias, A., & Kostoglodov, V. (2020). Scaling of Peak Ground Displacement with Seismic Moment above the Mexican Subduction Thrust. *Seismological Research Letters*.

Suzuki, W., Pulido, N., & Aoi, S. (2016). Rupture process and strong-motion generation of the 2014 Iquique, Northern Chile, earthquake. *Journal of Earthquake and Tsunami*, *10*(03), 1640008.

Vidale, J. E., Goes, S., & Richards, P. G. (1995). Near-field deformation seen on distant broadband seismograms. *Geophysical research letters*, *22*(1), 1-4.

Wang, R., Parolai, S., Ge, M., Jin, M., Walter, T. R., & Zschau, J. (2013). The 2011 M w 9.0 Tohoku earthquake: Comparison of GPS and strong-motion data. *Bulletin of the Seismological Society of America*, *103*(2B), 1336-1347.

Wyss, M., & Brune, J. N. (1968). Seismic moment, stress, and source dimensions for earthquakes in the California-Nevada region. *Journal of Geophysical Research*, *73*(14), 4681-4694.

Figures and Tables

Table S1. Location, type and magnitude of each earthquake used in this study.

Earthquake	Latitude	Longitude	Depth (Km)	Type	Magnitude
Antofagasta (1995)	23.360°S	70.310°W	47.0	Interplate	$M_w 8.0$
Tarapacá (2005)	19.895°S	69.125°W	108.0	Intraplate	$M_w 7.8$
Tocopilla (2007)	22.314°S	70.078°W	47.7	Interplate	$M_w 7.7$
Maule (2010)	36.290°S	73.239°W	30.0	Interplate	$M_w 8.8$
Iquique (2014)	19.572°S	70.908°W	38.9	Interplate	$M_w 8.2$
Iquique (2014)	20.545°S	70.418°W	26.1	Interplate	$M_w 7.6$
Illapel (2015)	31.553°S	71.864°W	11.1	Interplate	$M_w 8.3$
Chiloé (2016)	43.517°S	74.391°W	30.0	Interplate	$M_w 7.6$

Table S2. Strong-motion and GPS instrument and hypocentral distance.

Earthquake	Strong-motion	GNSS	Distance (Km)
Antofagasta (1995)	ANTO		
Tarapacá (2005)	PICA|		126.0
Tocopilla (2007)	PB04		60.9
Maule (2010)	CCSP	CONZ	69.7
	ROC1	ROBL	421.0
Iquique (2014)	PSGCX	PSGA	91.6
	PB11	PB11	138.2
Iquique (2014)	TA01	AEDA	36.0
Illapel (2015)	CO06	PFRJ	100.6
	CO03		136.8
Chiloé (2016)	GO07	QLLN	79.8

30 **Table S3.** Location of the PSGCX station and events used in Figure 9.

Station	Latitude	Longitude
PSGCX	-19.60°	-70.12°

31

Event	Latitude	Longitude	Depth (Km)	Magnitude (M_w)	St-Ev Distance (Km)
E1	-19.572°	-70.908°	38.9	8.2	91.6
E2	-20.545°	-70.418°	26.1	7.6	111.1
E3	-19.508°	-70.705°	39.0	6.5	80.1
E4	-20.413°	-70.186°	43.8	5.6	102.7
E5	-20.442°	-70.137°	46.0	4.4	101.0

32

33

34

35

36

37

38

39

40

41

42

43

44

45

46

47

48

49

50 **Table S4.** Seismic moment M_0, static displacement and PGD for GNSS records of the last
51 Chilean earthquakes.

Earthquake	M_0 **[N m]**	**Station**	**Static Displacement [m]**	**PGD [m]**	**Hypocentral Distance [Km]**
Antofagasta	1.2E+21	ANTO	0.50	0.55	50
Tocopilla	4.46E+20	CDLC	0.12	0.16	59
		SRGD	0.12	0.25	108
		VLZL	0.07	0.20	102
		JRGN	0.15	0.35	129
Maule	3.2E+22	CONZ	3.00	3.10	70
		CONS	5.00	5.20	133
		SJAV	2.40	2.60	159
		MAUL	1.10	1.30	226
Iquique	1.99E+21	PSGA	0.80	0.95	91
		ATJN	0.50	0.60	95
		PB11	0.40	0.60	139
		IQQE	0.30	0.45	119
		PB08	0.20	0.25	198
		PCHA	0.30	0.40	164
		MNMI	0.20	0.30	152
Iquique	4.46E+20	AEDA	0.20	0.26	36
		IQQE	0.17	0.30	49
Illapel	3.98E+21	PFRJ	1.30	1.50	100
		CNBA	1.20	1.20	42
		CMBA	0.80	0.85	91
		PEDR	0.50	0.60	135
		OVLL	0.65	0.80	121
		TOLO	0.25	0.35	182
Chiloé	3.16E+20,	QLLN	0.20	0.4	79

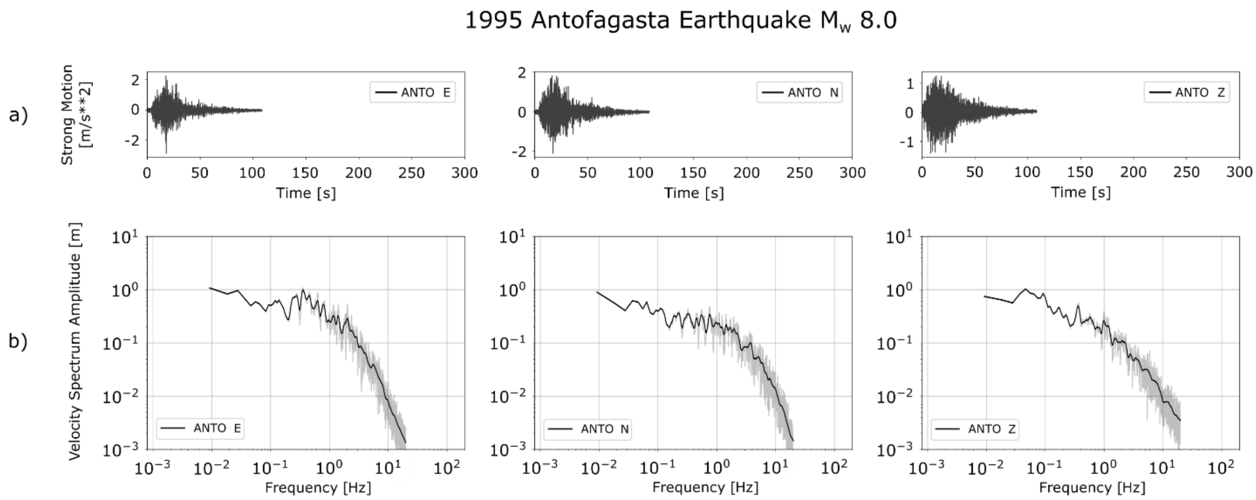

Figure S1. a) Three components of the acceleration records obtained at the ANTO station of the CSN network for the 31 July 1995 Antofagasta earthquake. **b)** Velocity spectrum computed from the acceleration record (black). Both spectra were smoothed with a Konno-Ohmachi filter.

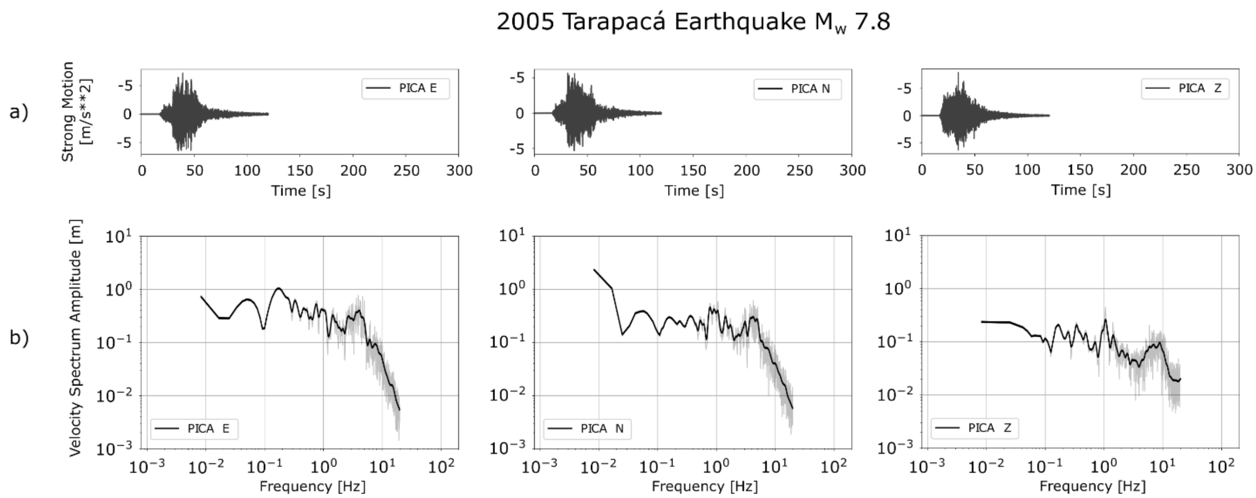

Figure S2. a) Three components of the acceleration records obtained at the PICA station of the CSN network for the 13 June 2005 Tarapacá earthquake. **b)** Velocity spectrum computed from the acceleration record (black). Both spectra were smoothed with a Konno-Ohmachi filter.

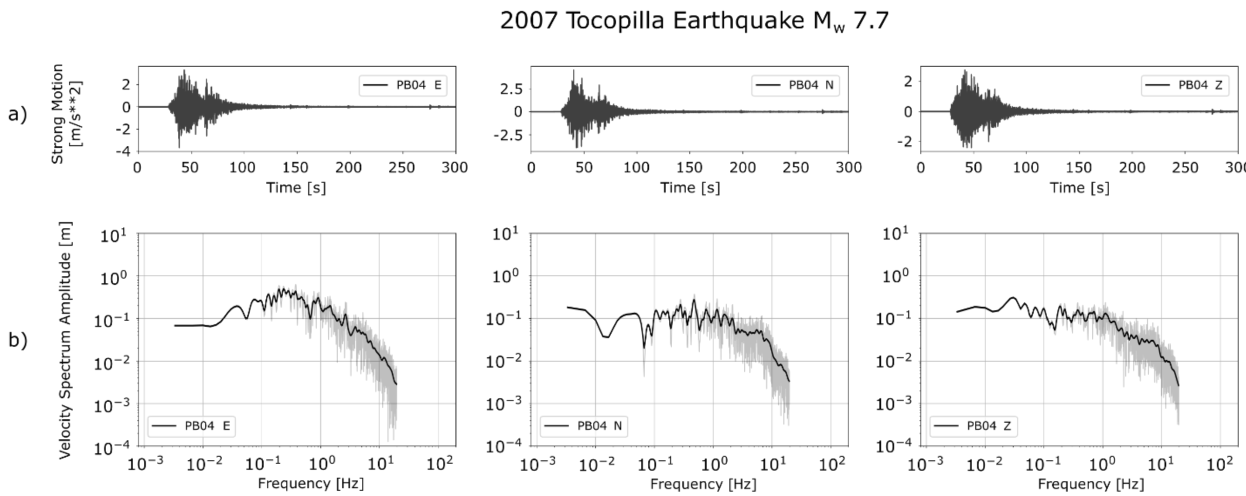

Figure S3. a) Three components of the acceleration records obtained at the PB04 station of the CSN network for the 14 October 2007 Tocopilla earthquake. **b)** Velocity spectrum computed from the acceleration record (black). Both spectra were smoothed with a Konno-Ohmachi filter.

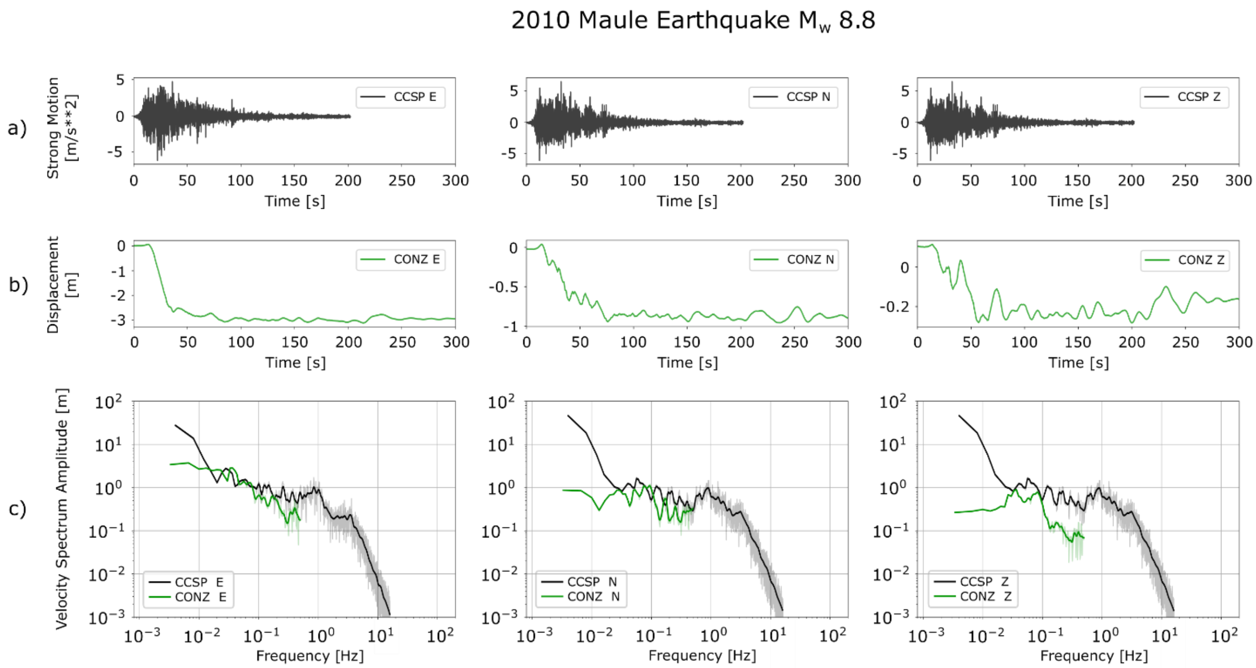

Figure S4. a) Three components of the acceleration records obtained at the CO06 station of the CSN network for the 27 February 2010 Maule earthquake. **b)** GNSS displacement at station PFRJ, collocated with the accelerometer. **c)** Velocity spectrum computed from the acceleration record (black) and from the displacement record (green). Both spectra were smoothed with a Konno-Ohmachi filter.

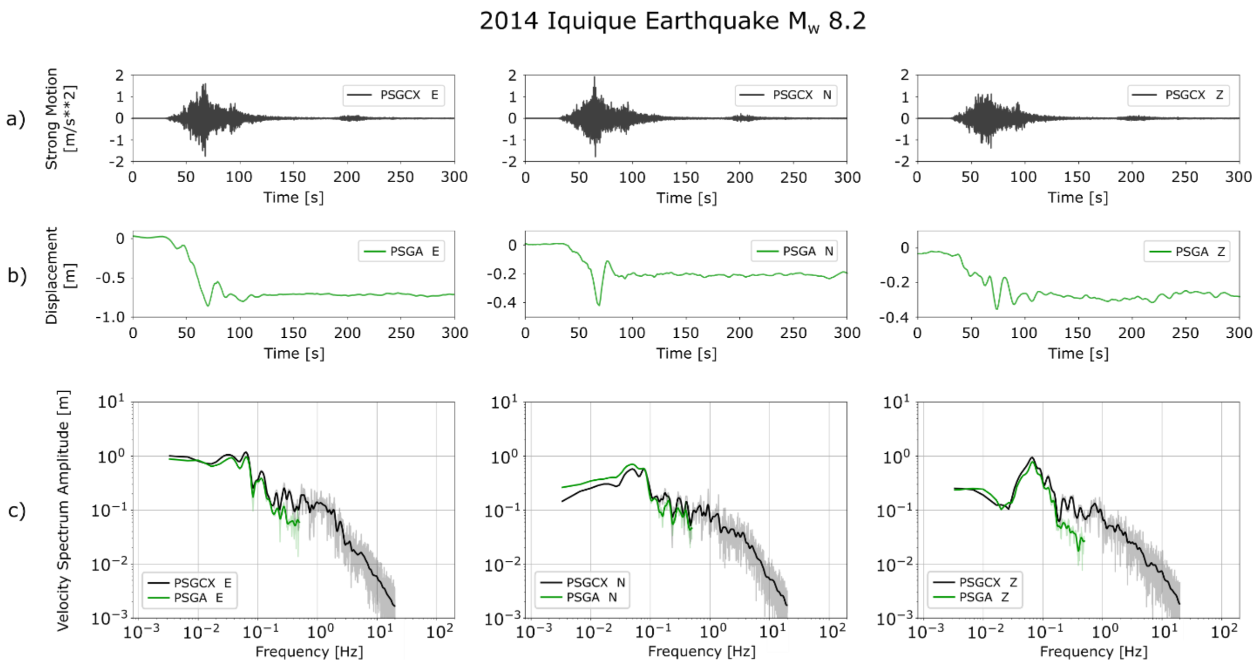

Figure S5. a) Three components of the acceleration records obtained at the CO06 station of the CSN network for the 1 April 2014 Iquique earthquake. **b)** GNSS displacement at station PFRJ, collocated with the accelerometer. **c)** Velocity spectrum computed from the acceleration record (black) and from the displacement record (green). Both spectra were smoothed with a Konno-Ohmachi filter.

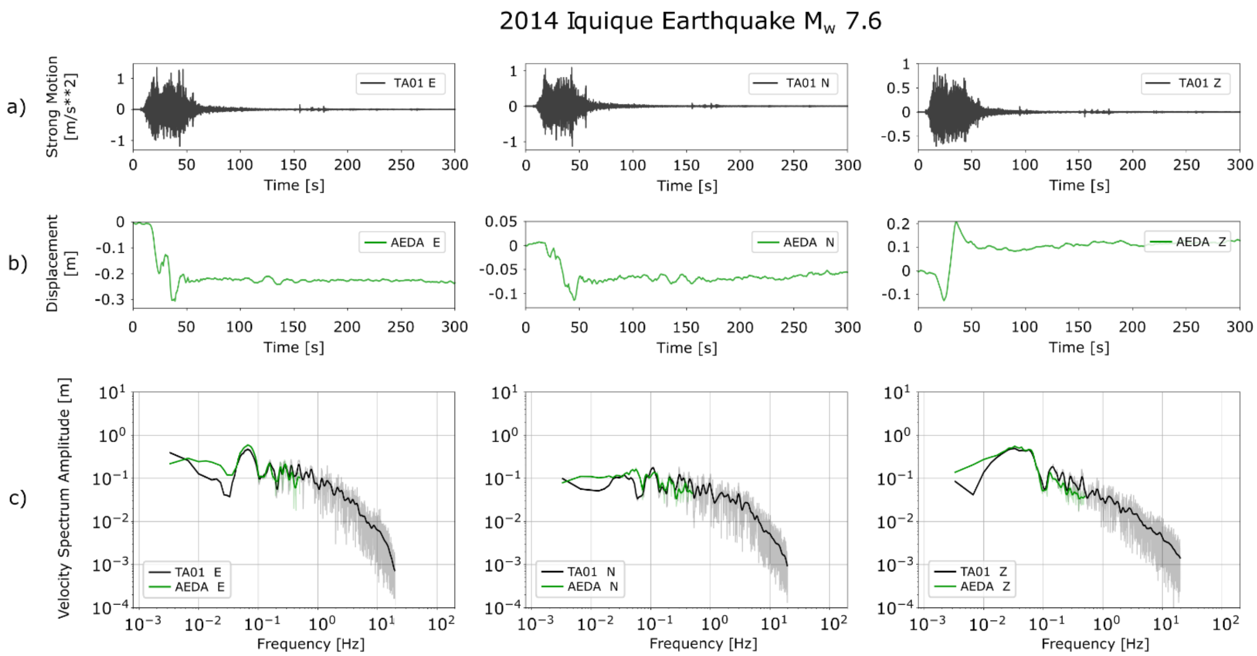

Figure S6. a) Three components of the acceleration records obtained at the CO06 station of the CSN network for the 3 April 2014 Iquique earthquake. **b)** GNSS displacement at station PFRJ, collocated with the accelerometer. **c)** Velocity spectrum computed from the acceleration record (black) and from the displacement record (green). Both spectra were smoothed with a Konno-Ohmachi filter.

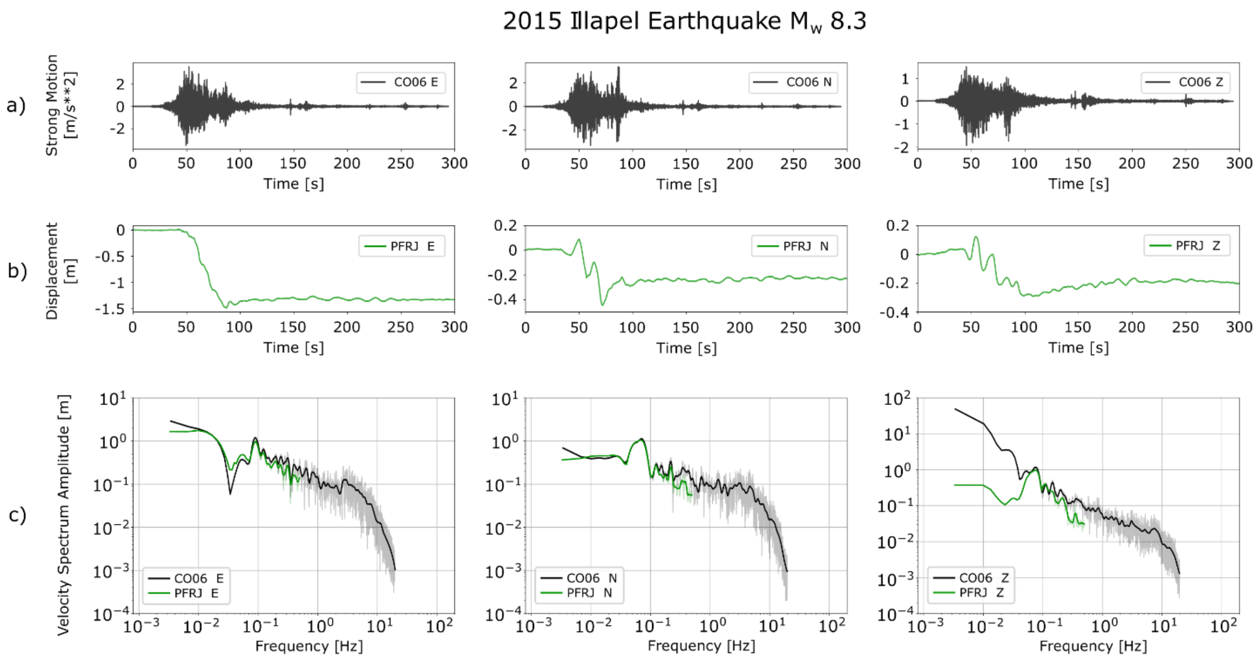

Figure S7. a) Three components of the acceleration records obtained at the CO06 station of the CSN network for the 16 September 2015 Illapel earthquake. **b)** GNSS displacement at station PFRJ, collocated with the accelerometer. **c)** Velocity spectrum computed from the acceleration record (black) and from the displacement record (green). Both spectra were smoothed with a Konno-Ohmachi filter.

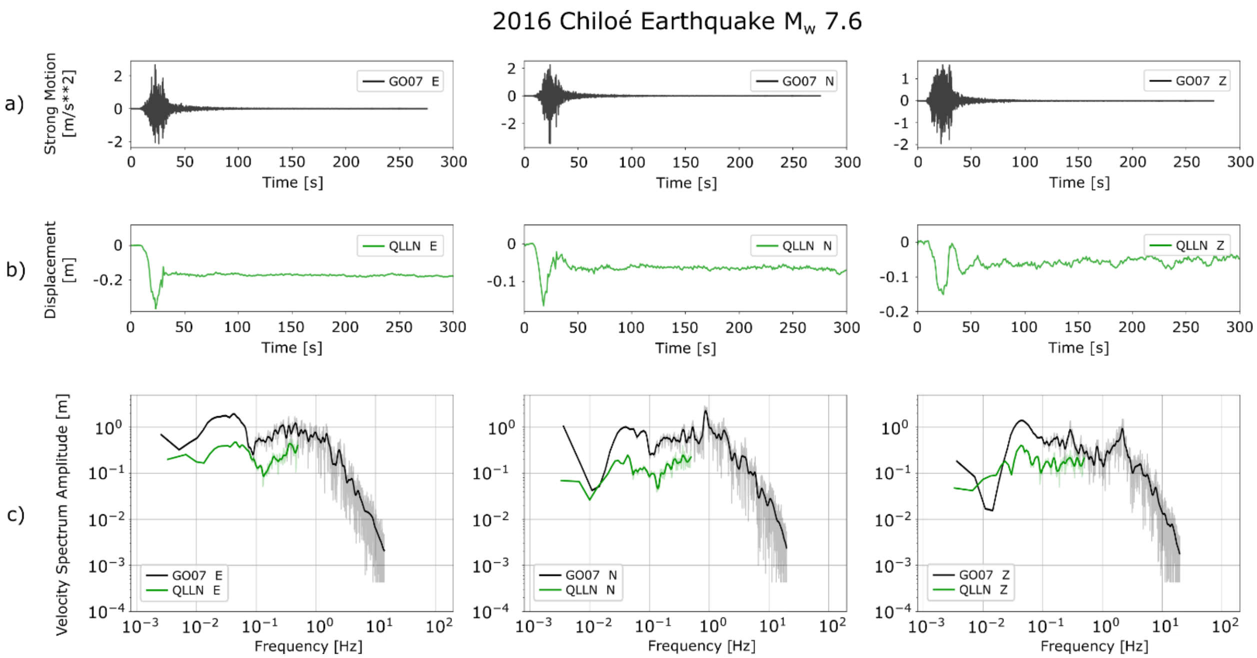

Figure S8. a) Three components of the acceleration records obtained at the CO06 station of the CSN network for the 25 December 2016 Chiloé earthquake. **b)** GNSS displacement at station PFRJ, collocated with the accelerometer. **c)** Velocity spectrum computed from the acceleration record (black) and from the displacement record (green). Both spectra were smoothed with a Konno-Ohmachi filter.